

Tinto: Multisensor Benchmark for 3D Hyperspectral Point Cloud Segmentation in the Geosciences

Ahmed J. Afifi, Samuel T. Thiele, Sandra Lorenz, Pedram Ghamisi, Raimon Tolosana-Delgado, Moritz Kirsch, Richard Gloaguen, Michael Heizmann

arXiv:2305.09928v1 [cs.CV] 17 May 2023

Abstract—The increasing use of deep learning techniques has reduced interpretation time and, ideally, reduced interpreter bias by automatically deriving geological maps from digital outcrop models. However, accurate validation of these automated mapping approaches is a significant challenge due to the subjective nature of geological mapping and the difficulty in collecting quantitative validation data. Additionally, many state-of-the-art deep learning methods are limited to 2D image data, which is insufficient for 3D digital outcrops, such as hyperclouds. To address these challenges, we present Tinto, a multi-sensor benchmark digital outcrop dataset designed to facilitate the development and validation of deep learning approaches for geological mapping, especially for non-structured 3D data like point clouds. Tinto comprises two complementary sets: 1) a real digital outcrop model from Corta Atalaya (Spain), with spectral attributes and ground-truth data, and 2) a synthetic twin that uses latent features in the original datasets to reconstruct realistic spectral data (including sensor noise and processing artifacts) from the ground-truth. The point cloud is dense and contains 3,242,964 labeled points. We used these datasets to explore the abilities of different deep learning approaches for automated geological mapping. By making Tinto publicly available, we hope to foster the development and adaptation of new deep learning tools for 3D applications in Earth sciences. The dataset can be accessed through this link: <https://doi.org/10.14278/rodare.2256>.

Index Terms—point cloud, hyperspectral, hypercloud, deep learning, point cloud segmentation, synthetic data, digital outcrop, remote sensing.

I. INTRODUCTION

THE need for annotated datasets to train and assess deep learning models has become essential in numerous advanced fields of research, including remote sensing and Earth observation [1]. Although there are several (ongoing) attempts to promote benchmarking and open science in the remote sensing field by developing exhaustive lists of available datasets [1, 2], evaluation servers (e.g., DASE¹), cloud services (e.g., Amazon Web Services², Microsoft’s Planetary Computer³, Radiant Earth’s MLHub⁴), and benchmark datasets

Ahmed J. Afifi, Samuel T. Thiele, Sandra Lorenz, Pedram Ghamisi, Raimon Tolosana-Delgado, Moritz Kirsch, and Richard Gloaguen are with the Helmholtz-Zentrum Dresden-Rossendorf (HZDR), Helmholtz Institute Freiberg for Resource Technology (HIF), 09599 Freiberg, Germany.

Ahmed J. Afifi & Michael Heizmann are with the Institute of Industrial Information Technology (IIIT), Karlsruhe Institute of Technology (KIT), 76187 Karlsruhe, Germany.

Pedram Ghamisi is also with the Institute of Advanced Research in Artificial Intelligence (IARAI), 1030 Vienna, Austria.

¹<http://dase.grss-ieee.org/>

²<https://registry.opendata.aws/>

³<https://planetarycomputer.microsoft.com/catalog>

⁴<https://www.mlhub.earth/>

(e.g., [3, 4, 5, 6]), novel applications within the fields of geomorphology, and geology remain sparse and unclear. Also, generally applicable reference data in remote sensing and geosciences for evaluating machine learning approaches are still not available in sufficient quantity and quality [7, 8].

Hyperspectral remote sensing has emerged as a powerful tool for detecting subtle spectral differences in mineralogical composition. The ability to apply this technology from a range of platforms, including satellites, airplanes, autonomous vehicles, and tripods, supports geological mapping at various scales. Integrating surface spectral data with topographic data enables the creation of hyperclouds, which are geometrically and radiometrically accurate point cloud representations of the target. Depending on the analysed range of the electromagnetic spectrum, a variety of minerals can be detected and mapped in their original 3D context. The visible and near-infrared (VNIR) and shortwave infrared range (SWIR) are useful for detecting spectral features of alteration minerals, such as oxides and hydroxides. In contrast, the long-wave infrared region (LWIR) allows for the detection of many rock-forming minerals, such as quartz and feldspars. Integrating both information sources enables comprehensive lithological mapping and has numerous geological applications, including greenfield exploration of critical raw materials, geological mapping of open-pit and underground mines, compositional mapping of rock wastes and stockpiles, and soil contamination mapping in post-mining landscapes.

Despite the vast potential of deep learning for hyperspectral mapping [9], it has found limited applicability for geoscientific applications, primarily due to the challenges associated with validation and the benchmarking of adapted algorithms [7]. Ground truth is difficult to establish for large-scale datasets, due to the limited accessibility of geological outcrops, their inherently complex and heterogeneous mineralogical composition as well as the traditionally rather subjective definition of lithological domains by geological experts based on mostly visual criteria. While simulated datasets have been used in the past, they do not yet capture the complexity and variability of real-world geological environments. The rather novel concept of 3D digital spectral outcrops (e.g., hyperclouds) is causing further complications due to the unstructured and complex nature of spectral point cloud data, which is incompatible with most state-of-the-art algorithms.

Geological scenes are preferred over highly structured scenes for benchmarking deep learning models in geosciences due to their complexity, variability, and real-world relevance. Geological scenes exhibit various features like rock forma-

tions, mineralogy, and topography, creating a realistic and challenging testing environment for deep learning algorithms. Class boundaries are diffused in the geological scenes and the classes are highly mixed. Benchmarking geological scenes enhance the models' generalization capability and learning new patterns and features from the training data, allowing them to adapt to new unseen geological scenarios and making them more robust and reliable in real-world applications. Additionally, it enables researchers to understand deep learning models' performance in capturing geological information and aligns with the needs of geoscientific applications. Overall, benchmarking on geological scenes provides a robust evaluation environment and facilitates tailored deep learning solutions in geosciences.

In this contribution, we present a large and geologically complex but well-understood real-world benchmark dataset, and a synthetic (reconstructed) equivalent, designed for testing and comparing deep learning methods for hyperspectral geological mapping. The real-world dataset covers Corta Atalaya, an abandoned open pit mine within the Minas de Rio Tinto copper mining district in Andalusia, Spain. The hyperspectral data have been acquired using plane, drone, and tripod-based acquisition and cover the VNIR, SWIR, and LWIR range of the electromagnetic spectrum. Lithology class labels have been defined for the whole dataset based on a combination of detailed laboratory analysis and derived supervised classification [10] and were adjusted based on an expert interpretation of the geology. However, due to the complex nature of geological datasets, this labeling cannot be treated with 100% confidence. To address this shortcoming, we used the real-world benchmark dataset to derive a realistic synthetic dataset in which class labels (and associated spectral endmembers and abundances) are known with certainty. This approach allows us to develop data for which the class and abundance properties are known with confidence while retaining the spatial statistical properties and complexity of a real dataset.

To facilitate established and emerging deep learning approaches, we present these datasets both in 2D raster form (as is conventional for remote sensing applications) and 3D point cloud form (for emerging approaches that are beginning to move beyond the topological limitations imposed by 2D rasters). Challenges and limitations associated with each data representation, and a selection of tools available for working with them, are discussed.

The rest of the paper is structured as follows. Section II reviews some related work and the available datasets for 3D point cloud processing. Section III describes the proposed Tinto benchmark dataset and how it is collected, labeled, and synthesised in detail. In Section IV, we discuss the baseline deep learning models that are used to evaluate the Tinto dataset, the experimental setup, and the experimental outcomes. Finally, the conclusion and remarks are drawn in Section V.

II. BACKGROUND AND RELATED WORK

A plethora of sophisticated methodologies has been advanced to segment 3D point clouds, often utilizing publicly

available datasets to evaluate their efficacy. These methodologies encompass a broad spectrum of techniques, from traditional methods to cutting-edge machine learning and deep learning approaches. In the following subsections, we provide a very brief overview of the mature field of diverse point cloud segmentation approaches by highlighting a few relevant examples and presenting a comprehensive collection of 3D datasets commonly employed for this specific task.

A. Point Cloud Segmentation

Traditional point cloud segmentation methods rely on strict hand-crafted geometric constraints and rules. The main goal of the segmentation process is to group 3D points into non-overlapping regions. The generated regions have common semantic meanings and geometric structures [11]. With the introduction of machine learning and deep learning models in solving 2D tasks and the availability of large-scale labeled datasets, many researchers proposed machine/deep learning models to segment point clouds from the object and scene levels. Generally, deep learning models achieved remarkable performance compared to traditional and machine learning methods. Following, we discuss different point cloud segmentation methods.

1) *Edge-based*: Edge-based methods try to detect points close to the edge by calculating the rapid changes in the intensity (the feature associated with the points) or the gradient. This will create boundaries between two different regions. Then, the points are grouped inside the same region where changes are small. These methods are fast but fail when the scene is dense or the point cloud is a scan of a large area because of the noise and the irregular points distribution [12, 13].

2) *Region growing*: Region growing-based methods involve the random selection of seed points and the measure of geometrical or feature similarity between the seeds and neighboring points. Points with similar features are merged to create one region. This process is performed iteratively until all points are merged into similar regions. These methods were firstly applied to 2.5D LiDAR data and they were widely applied for the segmentation of building structures. Similar points that belong to the same region can be selected by comparing their features or calculating the Euclidean similarity. The segmented points are selected for example by fitting a plane to a number of points in a given volume and then points with the minimum distance to that plane are merged [14, 15, 16].

3) *Shallow supervised Machine Learning*: Shallow supervised machine learning refers to non-deep algorithms that use labeled data to train a model. These methods allow classifying points in a cloud based on predefined features such as maximum likelihood based on support vector machine (SVM) [17], random forests (RF) [18], and Bayesian discriminant classifiers [19]. Other groups of methods depend on statistical contextual models such as Conditional Random Fields (CRF) [20] and Markov Random Fields (MRF) [21]. These methods focus on the statistics and the relational information of the points over different scales. Machine learning models applied

for point cloud segmentation perform a neighborhood point selection, then feature extraction from the grouped points, feature selection to reduce the feature dimensionality and then segment the points semantically.

4) *Deep Learning*: Deep Learning has become the most influential and hottest technique in different research fields such as computer vision, medical imaging, autonomous driving, and robotics. Deep Learning is a special branch of machine learning where the models are deeper, more complex and the extracted features generally have higher dimensions than the ones extracted from traditional machine learning methods. Applicable methods for applying deep learning on 3D data depend on how the data is represented. With multi-view data, a normal 2D Convolutional Neural Network (CNN) can be easily applied, such as the MVCNN model [22]. Voxel-based data can be used with 3D CNN, where the normal 2D CNN can be easily extended to 3D [23]. The drawback of using voxel-based representation is the memory and the computation cost to train a model. To overcome the voxel-based and multi-view methods, models that can be applied directly on point cloud data were recently proposed as a promising solution. Models applied directly on point clouds such as the pioneer model PointNet [24] were followed by the improved version PointNet++ [25] and the Dynamic Graph CNN (DGCNN) [26]. Other approaches of point cloud segmentation in the field of remote sensing and 3D laser scanning can be found in [27, 28, 29].

The research on point cloud segmentation using deep learning is a hot research topic. Different models are proposed with either sophisticated layers [30, 31, 32] to deal with the point cloud as an unordered set or with a simple architecture using MLP as a backbone of the model [33] to achieve improved performance with less computation and memory cost.

B. Available 3D Datasets

To our knowledge, no 3D hyperspectral benchmark datasets have been published for a geoscientific application context yet. Available benchmark datasets for point cloud segmentation deal with indoor scenes, such as Stanford Large-Scale 3D Indoor Spaces (S3DIS) [34] and Semantic3D.Net [35], or urban scenes, such as Sydney Urban Objects Dataset [36], Toronto-3D [37], and SemanticKITTI [38], for semantic segmentation. Other datasets focus on the objects, for instance segmentation or object parts segmentation, such as ShapeNet [5] and ModelNet40-C [39]. In most cases, point cloud attributes are limited to the 3D coordinates (X, Y, Z), intensity or RGB color values. The Maarmorilik Dataset [8] is an open-source 3D hyperspectral dataset capturing the complex geology of the Black Angel Mountain in Maarmorilik, West Greenland, alongside a detailed and interactive tutorial documenting relevant processing workflows for hypercloud data. It includes RGB and VNIR-SWIR hyperspectral data but does not provide ground truth and thus cannot be defined as a benchmark.

To the best of the authors' knowledge, the Tinto dataset will be the first-ever dataset that provides the following features: (1) a 3D point cloud of a real outcrop, (2) the corresponding ground truth, (3) the same scene captured using different

sensors (RGB, VNIR, SWIR, and LWIR), (4) hyperspectral information attached to each point in the point cloud, (5) two types of corresponding synthetic data (clean and noisy data), and (6) 2D views of the scene from three different directions.

III. TINTO DATASET

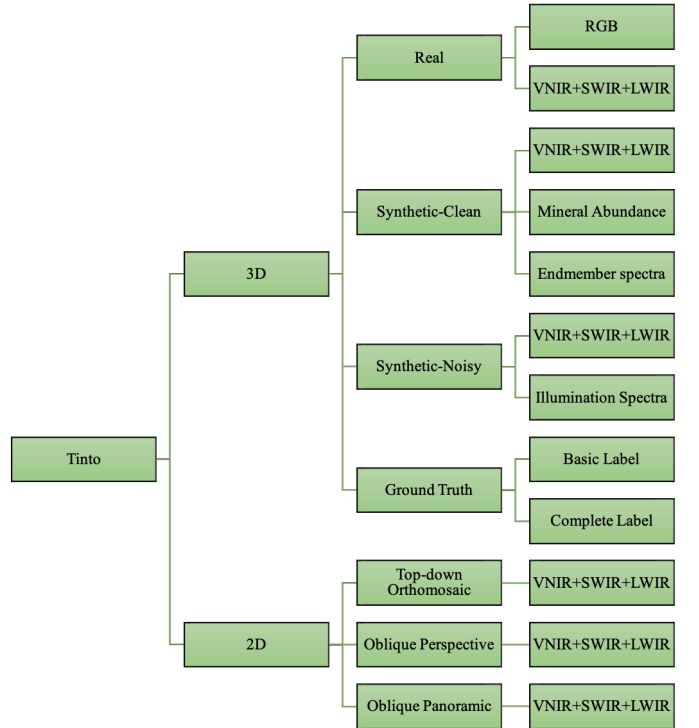


Fig. 1: An overview of the Tinto benchmark structure and the various datasets it contains.

A. Data Acquisition and Correction

Several steps of the acquisition and processing of the Corta Atalaya hyperclouds have been previously described by [10, 40]. To summarise briefly, a tripod-mounted hyperspectral Specim AisaFenix camera was used to capture oblique VNIR and SWIR imagery from three locations on the edge of the Corta Atalaya open-pit. Each of these rasters was then back-projected onto a dense 3D point cloud derived from 488 RGB photographs (captured using a Nikon D850 DSLR camera and Nikkor 85 mm f/1.8G lens) using the structure from motion multi-view stereo method implemented in Agisoft Metashape Professional v1.6. Atmospheric effects, which result largely from (i) the spectral signature of sunlight, (ii) interactions between this light and the atmosphere, and (iii) uneven illumination across the complex surface of the Corta Atalaya mine, were corrected using the method described by [41] during the back-projection step.

The long-wave infrared hyperspectral data was collected in August 2020 during a larger hyperspectral airborne mapping

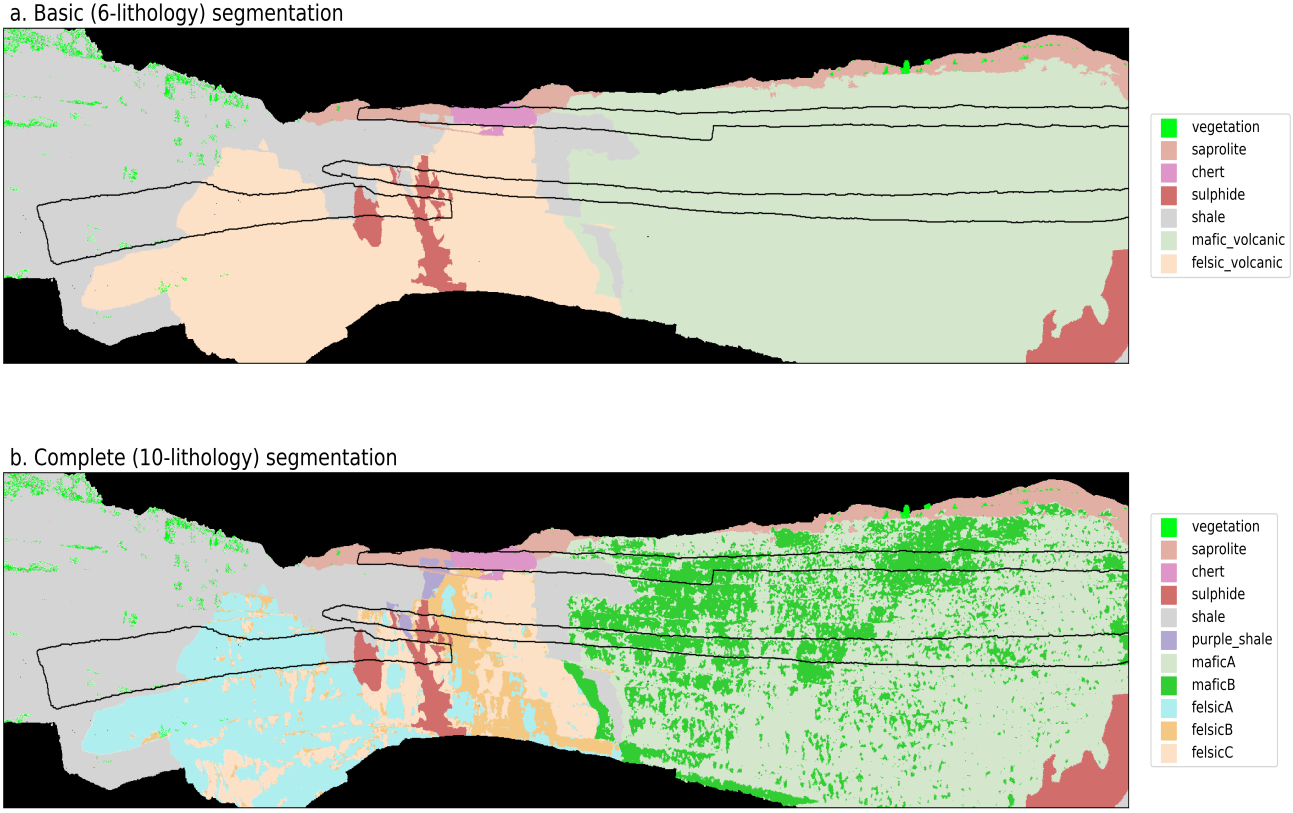


Fig. 2: Simplified (a) and complete (b) ground truth labels provided for this benchmark dataset. The suggested training subset is outlined in black and follows traverses that match roughly with how a field geologist would collect data.

campaign [40]. A Hyper-Cam FTIR hyperspectral camera from Telops was deployed, covering the electromagnetic spectrum between 7.7 and 11.8 micrometers. The collected raw data were processed using a standard workflow: The individual data cubes were orthorectified using a 2.5 m resolution Lidar-based terrain model, acquired within the same campaign, and subsequently stitched to a mosaic (average ground sampling distance of 1.2 m) using Telops' Reveal Airborne geolocation tool (version 2). Initial radiometric correction to at-sensor radiance was performed using the Telops Reveal Calibrate Software Version 5.2.8. Atmospheric correction was done by an In-Scene Atmospheric Compensation algorithm, while the separation of temperature and emissivity was performed based on emissivity normalization from the radiance data [40]. The resulting calibrated emissivity mosaic was then sampled onto the same dense 3D point cloud that was used with the VNIR-SWIR data to create an LWIR hypercloud to be included in this benchmark dataset. Figure 1 visualizes an overview of the Tinto benchmark dataset with the various datasets it contains [42]. The 3D visualization of the Tinto point clouds on Potree [43] can be accessed through this link: <https://www.hzdr.de/FWG/FWGE/Hyperclouds/Tinto.html>

B. Data labelling and synthetic twin

Geological maps, i.e., classifications that show the spatial distribution of rock types, are generally subjective interpretations of the map author due to (i) cover by vegetation or soil, (ii) ambiguous rock type definitions, and (iii) the thematic or purpose the author has in mind when creating the map. For example, a map intended to constrain geotechnical aspects of a mine would often differ significantly from one made to quantify the composition and distribution of ore, due to subjective choices made when defining and classifying different rock units. While this ambiguity is an important justification for automated methods offered by e.g., machine learning approaches, which can improve objectivity while simultaneously allowing for data to be reprocessed for various purposes, it presents significant challenges when developing meaningful and reliable benchmarks. In this contribution, we have mitigated these challenges using two radically different approaches: (1) deriving a manually vetted but largely data-driven classification for ground-truthing purposes, and (2) back-calculating a realistic dataset (synthetic twin) from this classification result to derive a hyperspectral dataset for which the original rock composition is known for each pixel. These two approaches are described in the following sections.

1) *Geological ground-truth*: In the first approach, which aims at a meaningful ground-truth classification for the real

hyperspectral data, we have integrated and synthesised hyperspectral information, sample mineralogy, field mapping and published geological understanding of Corta Atalaya. The spectral classification results of [10] were used as a base for the ground truth and manually corrected where field data, ground sampling and expert interpretation of the high-resolution photogrammetric model showed clear mislabelling. These results (Figure 2) were subsequently checked by mine geologists on-site, resulting in a labelled data set that we consider to be as accurate as practically possible for geological applications.

Several classes in this classification are spectrally and geologically related (e.g., classes defined by the presence of different but related alteration minerals; [10]). Lumping these together, we derive a simplified classification containing 6 rock types. While we encourage people to use the full label set, this simplified version could be useful for evaluating approaches that perform poorly with a large number of classes (e.g., unsupervised methods).

We have also defined a suggested training subset (Figure 2) to ensure consistent results between studies. This has been selected such that (1) it covers all classes in the dataset, and (2) matches with what could be realistically achieved in practice, with training data distributed along three bench-traverses that are typical for geological mapping in open-pit environments. Note that this geometry results in a highly imbalanced training set, a common challenge for hyperspectral classification problems. Table I and Table II present the number of points per class in the basic and complete ground truth, respectively.

TABLE I: Number of points per class in the training/testing split for the basic-label ground truth. Vegetation class is excluded during training and testing.

Class	Training	Testing	Color
Vegetation*	55,179		
Saprolite	28,231	309,540	
Chert	22,007	27,711	
Sulphide	13,095	128,264	
Shale	49,518	987,790	
Mafic_volcanic	143,861	1,037,782	
Felsic_volcanic	41,256	398,730	

TABLE II: Number of points per class in the training/testing split for the complete-label ground truth. Vegetation class is excluded during training and testing.

Class	Training	Testing	Color
Vegetation*	55,179		
Saprolite	28,229	309,263	
Chert	22,046	28,953	
Sulphide	13,066	129,085	
Shale	44,321	946,634	
Purple_shale	5,138	40,498	
MaficA	81,092	742,868	
MaficB	62,745	293,460	
FelsicA	20,790	166,804	
FelsicB	6,783	85,818	
FelsicC	13,758	146,434	

2) *Synthetic twin*: Potential issues associated with remaining biases or inconsistencies in the ground-truth labels have been addressed by generating an entirely synthetic suite of spectral data by forward modelling. These share the same labels as the real dataset, as well as several latent variables and spatial relationships, but are derived using a spectral mixing model and a spatial distribution of mineral abundances simulated using spectral proxies and sample measurements for each class from [10]. We suggest that these synthetic spectra are suited for comparing learning approaches, as the ground truth is known with certainty, while the real spectra can be used to evaluate performance on realistic data. The procedure followed to generate this synthetic twin is outlined below.

Firstly, three latent features known to correlate with specific mineral abundances (spectral proxies) were extracted from the real dataset using established minimum wavelength mapping and band-ratio techniques [10]. These were normalised to have a mean of zero and standard deviation of one and assembled into a vector \mathbf{L} containing the latent feature at every point, ensuring that spatial associations present in the real dataset (and potentially informative for deep machine learning methods) are preserved in the synthetic one.

Next, mineral abundances from x-ray diffraction measurements on the ground-truth samples [10] were used to define a mean composition for each class. To ensure the synthetic abundances sum to one, the so called additive log ratio transformation (ALR) [44] was used. As reference phase, an abundant phase was chosen, generally quartz. Sulphide was used for the massive sulphide class. Hence, the ALR transformed abundance α of the remaining phases was computed for each point x by

$$\alpha_{i,j}(x) = \log \left(\frac{\widehat{A}_{i,j}}{\widehat{A}_{0,j}} \right) + \sigma \mathbf{M}_i^T \cdot \mathbf{\Lambda}_j(x), \quad i = 1, 2, \dots, n \quad (1)$$

where $\widehat{A}_{i,j}$ denotes the average abundance of mineral $i \in \{0, 1, \dots, n\}$ in class j — $\widehat{A}_{0,j}$ being then the abundance of the reference mineral for class j —, the vector $\mathbf{\Lambda}_j(x)$ contains the values of the three latent variables described previously for class j at location x , and \mathbf{M}_i contains a manually defined mapping vector that determines the contribution of each latent variable to the log-abundance of the i -th mineral. Finally, σ scales the log standard deviation of the mineral abundances within each class, and was kept at a constant value of 0.3 after some experimentation.

A vector of closed abundances $\mathbf{A}(x)$ was then calculated for each point x by inverting the additive log transform [44]

$$\mathbf{A}_j(x) = \frac{\exp [0 \ \alpha_{1,j}(x) \ \dots \ \alpha_{n,j}(x)]}{\| \exp [0 \ \alpha_{1,j}(x) \ \dots \ \alpha_{n,j}(x)] \|_1}, \quad (2)$$

with $\exp(\cdot)$ the component-wise exponential function, resulting in a set of realistic mineral abundance maps (Figure 3). Following the real geology exposed in Corta Atalaya, a degree of endmember variability was then introduced by splitting the abundance of three mineral groups (muscovite, chlorite and clay) into compositional endmembers, based on the position of

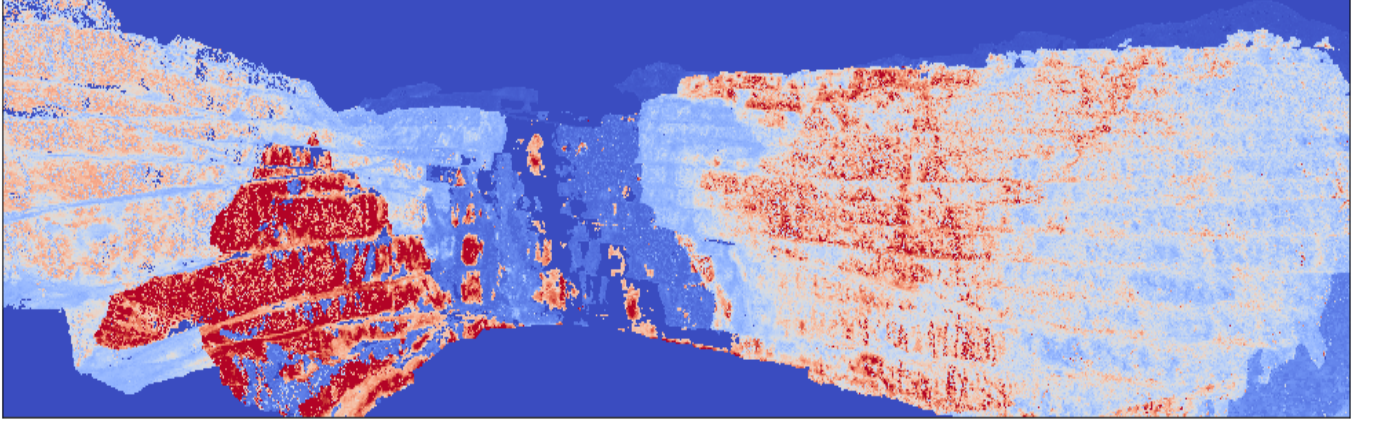


Fig. 3: Example of a simulated mineral abundance map (chlorite in this case). These were used to derive synthetic reflectance spectra with realistic spatial variations.

the 2200, 2250 and 2160 nm absorption features respectively. This extended the number of phases in \mathbf{A} from seven to ten, a realistic degree of complexity for geological outcrops. A pure endmember spectral library \mathbf{E} assembled using spectra from the USGS [45] was then used to derive a synthetic reflectance spectra \mathbf{S} for each data point, assuming linear mixing,

$$\mathbf{S} = \mathbf{E} \cdot \mathbf{A}. \quad (3)$$

These synthetic reflectance spectra, and the mineral abundances used to derive them, are also included in the benchmark dataset, and could be used for testing e.g., endmember identification and unmixing methods.

3) *Degraded twin*: In reality, sensor noise and other unwanted effects (e.g., atmospheric and topographic distortions, coating, vegetation) mean that no dataset will contain perfect reflectance spectra. Hence, as a final step, the synthetic reflectance spectra were degraded to simulate realistic measurement, preprocessing and data-correction procedures. First, the reflectance spectra were converted to at-target radiance estimates using the two-light-source atmospheric model described by [41] and the Oren-Nayar BRDF [46]. Simulating the real acquisition procedure, these radiance data were projected onto 2D rasters using three different camera poses, and path-radiance added to the corresponding spectra proportional to the target-sensor distance, resulting in three at-sensor radiance rasters. For the LWIR dataset, light emitted by the target (and by air between the target and the sensor) was also calculated, noting that $\text{emissivity} = 1 - \text{reflectance}$ following Kirchhoff's law, and added to the at-sensor radiance.

Each raster was then transformed according to the inverse of the sensor-specific lens calibration and converted to digital numbers by dividing by the lab-determined spectral calibration values. Sensor noise was added using dark-current data acquired during the acquisition of the real hyperspectral data, resulting in a set of three simulated raw rasters with realistic noise.

A degraded synthetic reflectance dataset (Figure 1) was then derived by correcting the simulated raw data using the same routine as was applied to the real data (cf., Section IIIA).

C. Accompanying 2D data

Although this manuscript focuses on 3-D point cloud data attributed with reflectance spectra to create hyperclouds, it is worth noting that we have included a set of 2-D rasters derived by projecting the class labels, real, synthetic and degraded spectra onto nadir, oblique perspective and oblique panoramic views (Figure 4). These will not be discussed further here, but could serve as a useful benchmark for image segmentation or unmixing methods.

IV. EVALUATION

A. Baseline Models

Many deep learning models designed for processing raw point clouds are primarily focused on classification and segmentation tasks. Point coordinates are typically the most common input to the network, and in some cases, normals and RGB values can also be incorporated. Many models proposed sophisticated layers to effectively process point clouds directly [30, 31, 32]. They learn the geometrical features of the points to perform the classification and segmentation tasks. Tinto dataset includes multiple sources of information, but the emphasis is on learning hyperspectral information for point cloud segmentation. To evaluate the Tinto dataset on deep learning models, three architectures designed for point cloud processing were selected and trained from scratch. A 10-layers Multi-Layer Perceptron (MLP) [47] was the first model implemented and tested on the dataset. Despite being simpler compared to other advanced deep models proposed for point cloud processing, the MLP performed comparably or even outperformed other models in some scenarios. The second model was PointNet [24], the first-ever model proposed for point cloud processing, while the third model was PointNet++ [25], its successor capable of extracting the local features of the point cloud. All the baseline models were modified and implemented to accept the hyperspectral information of a point as input for the segmentation task.

1) *Multi-Layer Perceptron (MLP)*: A neural network comprises a number of different layers of weighted neurons

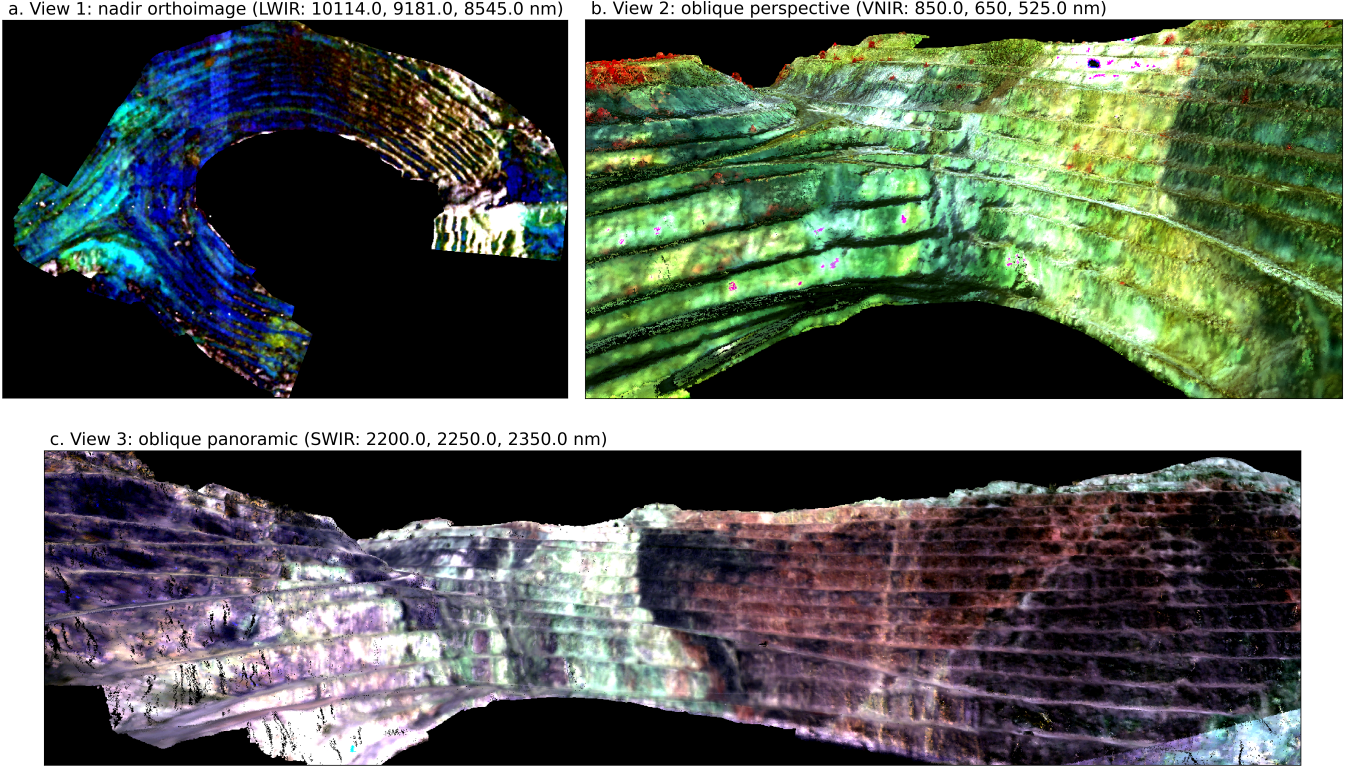


Fig. 4: False-colour visualisations of the real LWIR (a), VNIR (b) and SWIR (c) hyperspectral datasets from the three viewpoints used to derive the Tinto2D benchmark images.

through which activation is performed. MLP is a class of feedforward neural networks with two or more hidden layers between the input and the output layers. This network propagates the data in one direction from input to output layers. To optimize and adjust the network weights, a backpropagation algorithm is used to train the MLP. In our case, we implement the MLP to classify the point cloud according to its hyperspectral information. The output layer is equal to the number of classes. Our network consists of 10 hidden layers between the input and the output layers to extract useful features and help in the classification process. The hidden layers have to extract features of different sizes. The input layer takes the hyperspectral information of the point as input information. The output layer has the same size as the number of the classes in the ground-truth.

2) *PointNet*: Typical deep learning methods for 2D images are successful because of the convolution operation that learns the local structure in a hierarchical manner. However, the convolution operation needs to process data with a regular structure which is lacking in point cloud data representation. PointNet is a pioneering deep learning model that directly takes the point clouds as input and performs both classification and segmentation tasks. As the points are unordered in the point cloud data, PointNet is symmetrical or invariant to the points order. Specifically, PointNet applies point-wise operations using several MLP layers to extract independent features separately and uses max-pooling operation to capture

the global features of the point cloud. The aggregated global feature extracted from the point cloud can be used for various tasks such as classification and segmentation. The drawback of the PointNet model is that features are learned independently and then the global feature is aggregated. So, the local structure of the point cloud between points is not captured. Figure 5 presents the PointNet model.

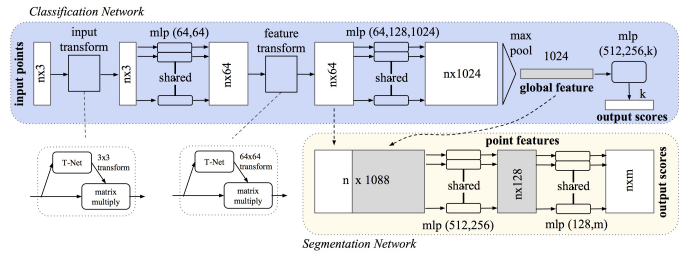


Fig. 5: PointNet architecture [24].

3) *PointNet++*: To overcome the drawback of the PointNet model in not capturing the local features of the point cloud, PointNet++ was proposed as a hierarchical network. PointNet++ consists of three main layers: the sampling layer, the grouping layer, and the PointNet based learning layer. The sampling layer uses the farthest point sampling algorithm to select centroids. The grouping layer uses the selected centroids to find the nearest neighbor points of each centroid. The PointNet layer is then applied on the local region to learn and extract the feature vector. This process is repeated in a

TABLE III: Performance of the baseline models on the proposed dataset. Numbers to the left are the accuracy for the basic labels. Numbers to the right are the accuracy for the complete labels.

Model	Real Data			Clean Synthetic Data			Noisy Synthetic Data		
	LWIR	SWIR	VNIR	LWIR	SWIR	VNIR	LWIR	SWIR	VNIR
MLP	59.8 / 43.0	85.1 / 73.4	76.8 / 62.6	99.0 / 92.4	99.0 / 93.3	99.0 / 90.4	88.5 / 75.6	87.5 / 77.8	85.5 / 74.3
PointNet	59.2 / 44.4	82.0 / 69.0	74.6 / 61.6	98.8 / 92.9	99.0 / 93.1	98.9 / 93.1	88.4 / 77.9	87.6 / 78.3	80.4 / 75.8
PointNet++	49.0 / 32.2	78.7 / 63.0	70.2 / 54.7	97.7 / 94.7	98.7 / 96.0	91.1 / 83.1	83.8 / 70.3	82.6 / 71.3	74.1 / 62.0

hierarchical form and the points' resolution is reduced as the network goes deeper. In the last layer the global feature is produced. Figure 6 presents the PointNet++ model.

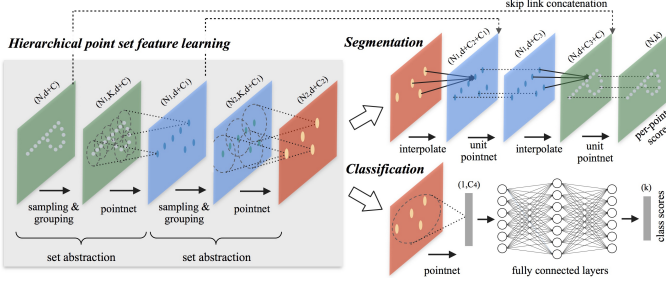


Fig. 6: PointNet++ architecture [25].

B. Implementation Details

We implemented, trained, and evaluated the baseline models on TensorFlow [48]. The dataset contains 3,187,785 points (excluding the Vegetation class). For the complete label scenario, the dataset is split into training set (297,968 points) and testing set (2,889,817 points) with the ratio of 10% and 90%, respectively. The inputs were the hyperspectral information of the points. The input size depends on the sensor used to acquire the data (VNIR = 51 bands, SWIR = 141 bands, and LWIR = 126 bands). The weights of the models were initialized using the Xavier initialization method [49]. We trained the models from scratch using an Adam optimizer [50] to optimize the network parameters with the following settings: the learning rate was set to 0.01, the momentum was set to 0.9, and the mini-batch size was 128 points. We trained the models until the validation accuracy stopped increasing. We excluded the Vegetation class during training and testing.

C. Experimental Results

We conducted experiments on the Tinto dataset to test the baseline models under different scenarios. All hyperspectral point clouds of the VNIR, SWIR, and LWIR (the real, clean synthetic, and noisy synthetic) for the complete and the basic labels are used for the evaluation.

Firstly, we trained the baseline models separately for each sensor data using the training set of real data with basic and complete labels. The trained models were then tested on the testing set, and their accuracy was calculated. The results indicated that the MLP model achieved the highest accuracy on the basic and complete labels except the complete label of the LWIR data where PointNet scored better accuracy. The PointNet++ model had the lowest accuracy with all sensors

in classifying the basic and complete labels when compared to the PointNet and MLP models. The original PointNet and PointNet++ models were designed to capture geometric information from shapes and performed well with objects and scenes that can be segmented into grids. These models mainly accept the coordinates of the points and other information (e.g., normals and RGB values) as input features to extract geometric information from the point cloud. However, since our dataset is represented by hyperspectral data, MLP models are better suited to extract useful information from the point cloud without guidance from the local coordinates of the points. Table III (Real Data) reports the overall accuracy of the baseline models on the real data for the basic and complete labels.

To address the issue of inaccurate ground truth labels, we proposed using the clean synthetic data where each point in the point cloud has a synthetic hyperspectral information. We trained the baseline models on the training set and evaluated them on the testing set from various sensors. We found that the model accuracies improved for the clean synthetic point cloud. Interestingly, the majority of models performed similarly on clean synthetic data from different hyperspectral sensors. We conclude that an accurate ground truth can significantly improve the model performance and segment the point cloud accurately. Table III (Clean Synthetic Data) reports the overall accuracy of the baseline models on the clean synthetic data for the basic and complete labels.

In order to increase the realism of the synthetic data and challenge the models further, we added real noise information (sensor noise and processing artifacts) to the synthetic point cloud. We evaluated the baseline models on the noisy synthetic data and found that their accuracy decreased compared to those trained on clean synthetic data. While all models achieved similar results, the PointNet model outperformed the other models on the noisy synthetic data on the complete labels and MLP outperformed the other models on the basic labels. PointNet++ scored an accuracy inferior to the MLP and PointNet in all scenarios. Table III (Noisy Synthetic Data) reports the overall accuracy of the baseline models on the noisy synthetic data for the basic and complete labels.

The results of the segmentation of SWIR data using the PointNet model are shown in Figure 7. We can see that PointNet struggles to generate the segmented point cloud from the real data depending on the hyperspectral information. PointNet scored accuracies of 82% and 69% for the basic and the complete labels, respectively. For the clean synthetic data, PointNet succeeded to segment the point cloud correctly with accuracies of 99% and 93.1% for the basic and the complete labels, respectively. For the noisy synthetic data, the real noise

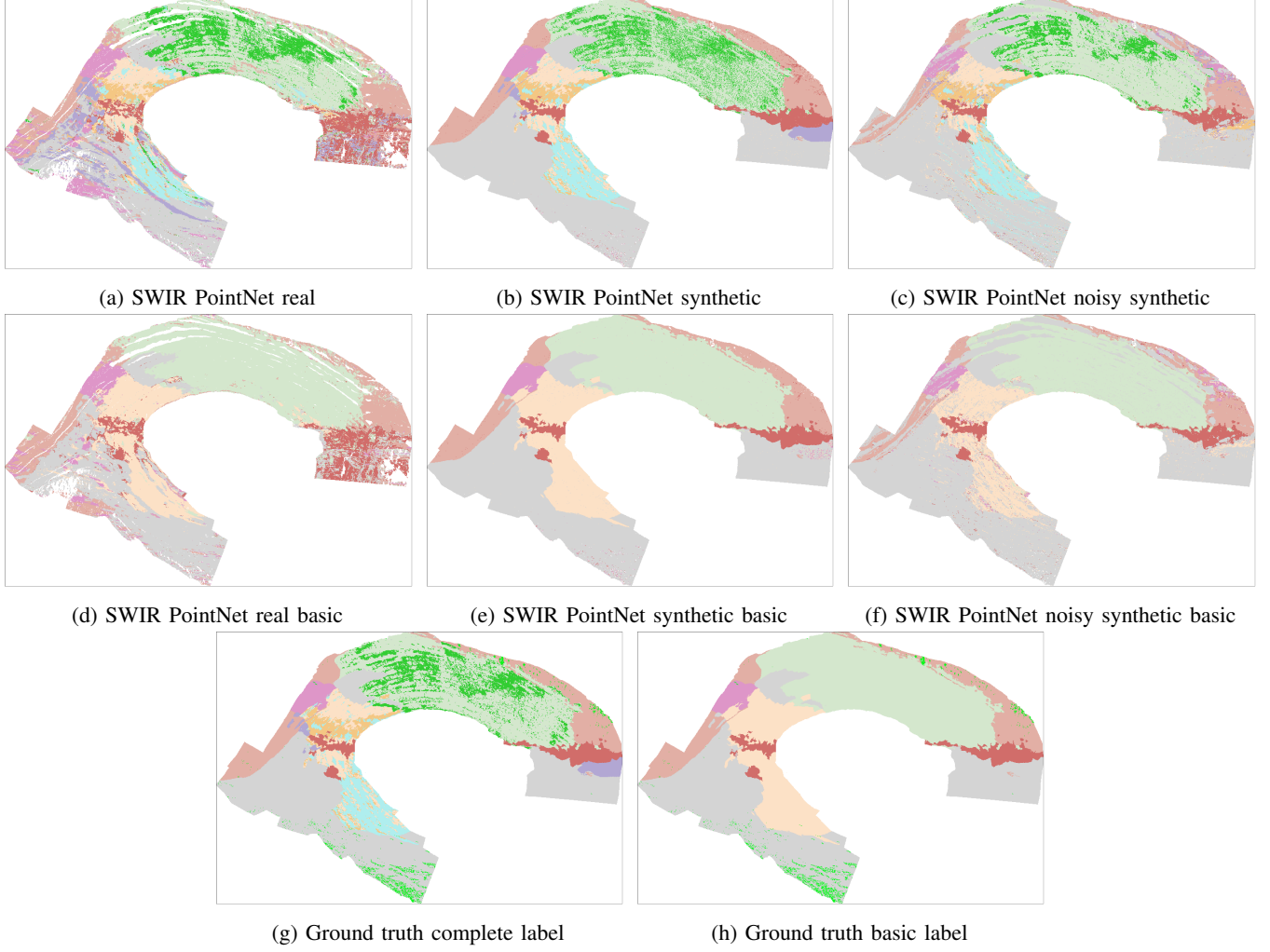


Fig. 7: Segmentation Results of the SWIR data in different scenarios inferred by PointNet.

was added to the point cloud to emulate the real scenario of the dataset. PointNet's performance improved by around 5% and 9% compared to the results on real data, with accuracy scores of 87.6% and 78.3% for the basic and complete labels, respectively. These findings suggest that it is possible to utilize hyperspectral information in the point cloud to train deep learning models for geological applications.

V. CONCLUSION

This paper introduced the first-ever fully-labeled multi-sensor hyperspectral benchmark dataset that is a valuable resource for researchers working on point cloud segmentation in geosciences. The dataset is comprehensive and diverse, covering real and synthetic data with different level of labelling for the classes. The Tinto dataset is a suitable benchmark for developing and evaluating point cloud segmentation algorithms for the geological applications. We believe that this dataset will serve as a benchmark for future studies and contribute to the development of innovative solutions for point cloud segmentation in geosciences. Overall, the Tinto benchmark dataset represents a significant contribution to the field and holds promise for a broad range of applications in

mineral exploration, geological mapping, and natural resource management.

ACKNOWLEDGMENT

The authors would like to acknowledge extensive support from Atalaya Mining during fieldwork conducted for this publication, and subsequent validation of the results. This research received funding from the Initiative and Networking Fund (INF) of the Hermann von Helmholtz Association of German Research Centres in the framework of the Helmholtz Imaging Platform (HIP) under grant agreement No ZT-I-PF-4-021 and from the European Union's Horizon 2020 research and innovation programme under grant agreement No 776487.

REFERENCES

- [1] M. Schmitt, P. Ghamisi, N. Yokoya, and R. Hänsch, “Eod: The ieee grss earth observation database,” in *IGARSS 2022 - 2022 IEEE International Geoscience and Remote Sensing Symposium*, 2022, pp. 5365–5368.
- [2] C. Rieke, “Awesome satellite imagery datasets,” <https://github.com/chriek/awesome-satellite-imagery-datasets>, 2022.

[3] O. Ghorbanzadeh, Y. Xu, P. Ghamisi, M. Kopp, and D. Kreil, "Landslide4sense: Reference benchmark data and deep learning models for landslide detection," *IEEE Transactions on Geoscience and Remote Sensing*, vol. 60, pp. 1–17, 2022.

[4] J. A. Hurt, G. J. Scott, D. T. Anderson, and C. H. Davis, "Benchmark meta-dataset of high-resolution remote sensing imagery for training robust deep learning models in machine-assisted visual analytics," in *2018 IEEE Applied Imagery Pattern Recognition Workshop (AIPR)*, 2018, pp. 1–9.

[5] A. X. Chang, T. Funkhouser, L. Guibas, P. Hanrahan, Q. Huang, Z. Li, S. Savarese, M. Savva, S. Song, H. Su *et al.*, "Shapenet: An information-rich 3d model repository," *arXiv preprint arXiv:1512.03012*, 2015.

[6] G. Sumbul, M. Charfuelan, B. Demir, and V. Markl, "Bigearthnet: A large-scale benchmark archive for remote sensing image understanding," in *IGARSS 2019-2019 IEEE International Geoscience and Remote Sensing Symposium*. IEEE, 2019, pp. 5901–5904.

[7] P. Ghamisi, K. R. Shahi, P. Duan, B. Rasti, S. Lorenz, R. Booysen, S. Thiele, I. C. Contreras, M. Kirsch, and R. Gloaguen, "The potential of machine learning for a more responsible sourcing of critical raw materials," *IEEE Journal of Selected Topics in Applied Earth Observations and Remote Sensing*, vol. 14, pp. 8971–8988, 2021.

[8] S. Lorenz, S. T. Thiele, M. Kirsch, G. Unger, R. Zimmermann, P. Guarneri, N. Baker, E. V. Sørensen, D. Rosa, and R. Gloaguen, "Three-dimensional, km-scale hyperspectral data of well-exposed zn–pb mineralization at black angel mountain, greenland," *Data*, vol. 7, no. 8, p. 104, 2022.

[9] S. Li, W. Song, L. Fang, Y. Chen, P. Ghamisi, and J. A. Benediktsson, "Deep learning for hyperspectral image classification: An overview," *IEEE Transactions on Geoscience and Remote Sensing*, vol. 57, no. 9, pp. 6690–6709, 2019.

[10] S. T. Thiele, S. Lorenz, M. Kirsch, I. C. C. Acosta, L. Tusa, E. Herrmann, R. Möckel, and R. Gloaguen, "Multi-scale, multi-sensor data integration for automated 3-d geological mapping," *Ore Geology Reviews*, vol. 136, p. 104252, 2021.

[11] Y. Xie, J. Tian, and X. X. Zhu, "Linking points with labels in 3d: A review of point cloud semantic segmentation," *IEEE Geoscience and remote sensing magazine*, vol. 8, no. 4, pp. 38–59, 2020.

[12] T. Rabbani, F. Van Den Heuvel, and G. Vosselmann, "Segmentation of point clouds using smoothness constraint," *International archives of photogrammetry, remote sensing and spatial information sciences*, vol. 36, no. 5, pp. 248–253, 2006.

[13] A. D. Sappa and M. Devy, "Fast range image segmentation by an edge detection strategy," in *Proceedings Third International Conference on 3-D Digital Imaging and Modeling*. IEEE, 2001, pp. 292–299.

[14] P. J. Besl and R. C. Jain, "Segmentation through variable-order surface fitting," *IEEE Transactions on pattern analysis and machine intelligence*, vol. 10, no. 2, pp. 167–192, 1988.

[15] A.-V. Vo, L. Truong-Hong, D. F. Laefer, and M. Bertolotto, "Octree-based region growing for point cloud segmentation," *ISPRS Journal of Photogrammetry and Remote Sensing*, vol. 104, pp. 88–100, 2015.

[16] A. Nurunnabi, D. Belton, and G. West, "Robust segmentation in laser scanning 3d point cloud data," in *2012 International Conference on Digital Image Computing Techniques and Applications (DICTA)*. IEEE, 2012, pp. 1–8.

[17] J. Zhang, X. Lin, and X. Ning, "Svm-based classification of segmented airborne lidar point clouds in urban areas," *Remote sensing*, vol. 5, no. 8, pp. 3749–3775, 2013.

[18] N. Chehata, L. Guo, and C. Mallet, "Airborne lidar feature selection for urban classification using random forests," in *Laserscanning*, 2009.

[19] S. Srivastava, M. R. Gupta, and B. A. Frigyik, "Bayesian quadratic discriminant analysis," *Journal of Machine Learning Research*, vol. 8, no. 6, 2007.

[20] E. H. Lim and D. Suter, "3d terrestrial lidar classifications with super-voxels and multi-scale conditional random fields," *Computer-Aided Design*, vol. 41, no. 10, pp. 701–710, 2009.

[21] Y. Lu and C. Rasmussen, "Simplified markov random fields for efficient semantic labeling of 3d point clouds," in *2012 IEEE/RSJ International Conference on Intelligent Robots and Systems*. IEEE, 2012, pp. 2690–2697.

[22] H. Su, S. Maji, E. Kalogerakis, and E. Learned-Miller, "Multi-view convolutional neural networks for 3d shape recognition," in *Proceedings of the IEEE international conference on computer vision*, 2015, pp. 945–953.

[23] D. Maturana and S. Scherer, "Voxnet: A 3d convolutional neural network for real-time object recognition," in *2015 IEEE/RSJ international conference on intelligent robots and systems (IROS)*. IEEE, 2015, pp. 922–928.

[24] C. R. Qi, H. Su, K. Mo, and L. J. Guibas, "Pointnet: Deep learning on point sets for 3d classification and segmentation," in *Proceedings of the IEEE conference on computer vision and pattern recognition*, 2017, pp. 652–660.

[25] C. R. Qi, L. Yi, H. Su, and L. J. Guibas, "Pointnet++: Deep hierarchical feature learning on point sets in a metric space," *Advances in neural information processing systems*, vol. 30, 2017.

[26] Y. Wang, Y. Sun, Z. Liu, S. E. Sarma, M. M. Bronstein, and J. M. Solomon, "Dynamic graph cnn for learning on point clouds," *Acm Transactions On Graphics (tog)*, vol. 38, no. 5, pp. 1–12, 2019.

[27] Y. Lin, G. Vosselman, and M. Y. Yang, "Weakly supervised semantic segmentation of airborne laser scanning point clouds," *ISPRS journal of photogrammetry and remote sensing*, vol. 187, pp. 79–100, 2022.

[28] R. Huang, Y. Xu, and U. Stilla, "Granet: Global relation-aware attentional network for semantic segmentation of als point clouds," *ISPRS Journal of Photogrammetry and Remote Sensing*, vol. 177, pp. 1–20, 2021.

[29] Y. Lin, G. Vosselman, Y. Cao, and M. Y. Yang, "Local

and global encoder network for semantic segmentation of airborne laser scanning point clouds,” *ISPRS journal of photogrammetry and remote sensing*, vol. 176, pp. 151–168, 2021.

[30] W. Wu, Z. Qi, and L. Fuxin, “Pointconv: Deep convolutional networks on 3d point clouds,” in *Proceedings of the IEEE/CVF Conference on computer vision and pattern recognition*, 2019, pp. 9621–9630.

[31] Y. Li, R. Bu, M. Sun, W. Wu, X. Di, and B. Chen, “Pointcnn: Convolution on x-transformed points,” *Advances in neural information processing systems*, vol. 31, 2018.

[32] G. Cai, Z. Jiang, Z. Wang, S. Huang, K. Chen, X. Ge, and Y. Wu, “Spatial aggregation net: Point cloud semantic segmentation based on multi-directional convolution,” *Sensors*, vol. 19, no. 19, p. 4329, 2019.

[33] X. Ma, C. Qin, H. You, H. Ran, and Y. Fu, “Rethinking network design and local geometry in point cloud: A simple residual mlp framework,” *arXiv preprint arXiv:2202.07123*, 2022.

[34] Q. Xu, X. Sun, C.-Y. Wu, P. Wang, and U. Neumann, “Grid-gcn for fast and scalable point cloud learning,” in *Proceedings of the IEEE/CVF Conference on Computer Vision and Pattern Recognition*, 2020, pp. 5661–5670.

[35] T. Hackel, N. Savinov, L. Ladicky, J. D. Wegner, K. Schindler, and M. Pollefeys, “Semantic3d.net: A new large-scale point cloud classification benchmark,” *arXiv preprint arXiv:1704.03847*, 2017.

[36] A. Quadros, J. P. Underwood, and B. Douillard, “An occlusion-aware feature for range images,” in *2012 IEEE International Conference on Robotics and Automation*. IEEE, 2012, pp. 4428–4435.

[37] W. Tan, N. Qin, L. Ma, Y. Li, J. Du, G. Cai, K. Yang, and J. Li, “Toronto-3D: A large-scale mobile lidar dataset for semantic segmentation of urban roadways,” in *Proceedings of the IEEE/CVF Conference on Computer Vision and Pattern Recognition Workshops*, 2020, pp. 202–203.

[38] J. Behley, M. Garbade, A. Milioto, J. Quenzel, S. Behnke, C. Stachniss, and J. Gall, “SemanticKITTI: A Dataset for Semantic Scene Understanding of LiDAR Sequences,” in *Proc. of the IEEE/CVF International Conf. on Computer Vision (ICCV)*, 2019.

[39] J. Sun, Q. Zhang, B. Kailkhura, Z. Yu, C. Xiao, and Z. M. Mao, “Benchmarking robustness of 3d point cloud recognition against common corruptions,” *arXiv preprint arXiv:2201.12296*, 2022.

[40] M. Kirsch, S. Lorenz, S. Thiele, and R. Gloaguen, “Characterisation of massive sulphide deposits in the iberian pyrite belt based on the integration of digital outcrops and multi-scale, multi-source hyperspectral data,” in *2021 IEEE International Geoscience and Remote Sensing Symposium IGARSS*. IEEE, 2021, pp. 126–129.

[41] S. T. Thiele, S. Lorenz, M. Kirsch, and R. Gloaguen, “A novel and open-source illumination correction for hyperspectral digital outcrop models,” *IEEE Transactions on Geoscience and Remote Sensing*, vol. 60, pp. 1–12, 2021.

[42] A. J. Afifi, S. T. Thiele, S. Lorenz, P. Ghamisi, R. Tolosana-Delgado, M. Kirsch, R. Gloaguen, and M. Heizmann, “Tinto: Multisensor Benchmark for 3D Hyperspectral Point Cloud Segmentation in the Geosciences,” Apr. 2023. [Online]. Available: <https://doi.org/10.14278/rodare.2256>

[43] M. Schütz *et al.*, “Potree: Rendering large point clouds in web browsers,” *Technische Universität Wien, Wieden*, 2016.

[44] J. Aitchison, *The Statistical Analysis of Compositional Data*, ser. Monographs on Statistics and Applied Probability. London (UK): Chapman & Hall Ltd. (Reprinted in 2003 with additional material by The Blackburn Press), 1986, 416 p.

[45] R. Kokaly, R. Clark, G. Swayze, K. Livo, T. Hoefen, N. Pearson, R. Wise, W. Benzel, H. Lowers, R. Driscoll *et al.*, “Usgs spectral library version 7 data: Us geological survey data release,” *United States Geological Survey (USGS): Reston, VA, USA*, 2017.

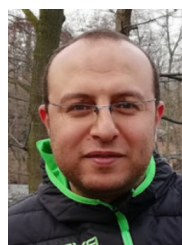
[46] M. Oren and S. K. Nayar, “Generalization of lambert’s reflectance model,” in *Proceedings of the 21st annual conference on Computer graphics and interactive techniques*, 1994, pp. 239–246.

[47] M.-C. Popescu, V. E. Balas, L. Perescu-Popescu, and N. Mastorakis, “Multilayer perceptron and neural networks,” *WSEAS Transactions on Circuits and Systems*, vol. 8, no. 7, pp. 579–588, 2009.

[48] M. Abadi, P. Barham, J. Chen, Z. Chen, A. Davis, J. Dean, M. Devin, S. Ghemawat, G. Irving, M. Isard *et al.*, “Tensorflow: a system for large-scale machine learning.” in *Osdi*, vol. 16, no. 2016. Savannah, GA, USA, 2016, pp. 265–283.

[49] X. Glorot and Y. Bengio, “Understanding the difficulty of training deep feedforward neural networks,” in *Proceedings of the thirteenth international conference on artificial intelligence and statistics*. JMLR Workshop and Conference Proceedings, 2010, pp. 249–256.

[50] D. P. Kingma and J. Ba, “Adam: A method for stochastic optimization,” *arXiv preprint arXiv:1412.6980*, 2014.



Ahmed J. Afifi received the bachelor’s and M.Sc. degrees in computer engineering from the Islamic University of Gaza (IUG), in 2008 and 2011, respectively. He completed his Ph.D. degree (Dr.-Ing.) at Technische Universität Berlin, Germany in 2021. Currently, he is a postdoctoral researcher with Helmholtz-Institute Freiberg for Resource Technology (HIF) and Karlsruhe Institute of Technology (KIT) where he is working on 3D point cloud classification and segmentation. His research interests include computer vision, deep learning, 3D object reconstruction from a single image, and medical image analysis.



Samuel T. Thiele received his M.Sc in Geology from the University of Western Australia in Perth. Following this, he was awarded a Westpac Future Leader scholarship to pursue a PhD project on the application of digital mapping technologies to volcanic landslides and magma plumbing systems. Since 2019 he has worked at the Helmholtz-Institute Freiberg for Resource Technology, with a focus on outcrop and drillcore hyperspectral remote sensing techniques and their application to minerals exploration and digital outcrop mapping.



Sandra Lorenz is research associate at the Helmholtz-Institute Freiberg for Resource Technology, where she currently leads the research group for Digital Processing within the Department of Exploration. She received the Ph.D. degree “Doctor rerum naturalis” in Geosciences at the Technical University Bergakademie Freiberg, Germany in 2019. Her main research interest lies in the development of spectral imaging as non-invasive material characterisation method at different scales, with a particular focus on spectral image and point-cloud processing and the implementation of autonomous platforms for hyperspectral surveys.



Pedram Ghamisi (Senior Member, IEEE) graduated with a Ph.D. in electrical and computer engineering from the University of Iceland. He currently works as the head of the machine learning group at the Helmholtz-Institute Freiberg for Resource Technology in Germany and as a research professor and senior PI (leader of AI4RS) at the Institute of Advanced Research in Artificial Intelligence (IARAI) in Austria. He specializes in deep learning for remote sensing applications.



Raimon Tolosana-Delgado is engineering geologist by the University of Barcelona and Technical University of Catalonia, Barcelona (Spain), doctor in environmental physics and technology by the University of Girona (Spain) and got a professoral qualification in mathematical geosciences by the Technische Universität Bergakademie Freiberg (Germany). He is specialist in geostatistics and compositional data analysis, and works at the Helmholtz-Institute Freiberg for Resource Technology applying stochastic modelling and data analysis to ore body modelling, geometallurgy and minerals processing modelling.



Moritz Kirsch received his M.Sc. in Geology from the Technische Universität Bergakademie Freiberg, Germany, in 2008 and his Ph.D. from the Universidad Nacional Autónoma de México in 2012. Since 2016, he has been working as a research associate at the Helmholtz Institute Freiberg for Resource Technology (HIF), Helmholtz-Zentrum Dresden-Rossendorf, where he leads a group on Innovative Applications in the Department of Exploration. His research interests lie at the intersection of geology and technology, with a focus on leveraging the latest digital tools, such as hyperspectral imaging and 3D modelling, to characterise mineral assemblages and understand geological processes.



Richard Gloaguen Head of the Exploration Department at the Helmholtz-Institute Freiberg for Resource Technology. Richard Gloaguen received the Ph.D. degree “Doctor Communitatis Europae” in marine geosciences from the University of Western Brittany, Brest, France, in collaboration with the Royal Holloway University of London, U.K., and Göttingen University, Germany, in 2000. He was a Marie Curie Post-Doctoral Research Associate at the Royal Holloway University of London from 2000 to 2003. He led the Remote Sensing Group at University Bergakademie Freiberg, Freiberg, Germany, from 2003 to 2013. Since 2013, he has been leading the division “Exploration Technology” at the Helmholtz-Institute Freiberg for Resource Technology, Freiberg. He is currently involved in UAV-based multisource imaging, laser-induced fluorescence, and non-invasive exploration. His research interests focus on multisource and multiscale remote sensing integration using computer vision and machine learning.



Michael Heizmann received the M.Sc. degree in mechanical engineering and the Ph.D. degree in automated visual inspection from the University of Karlsruhe, Germany, in 1998 and 2004, respectively. Since 2016, he has been a Full Professor in mechatronic measurement systems and the Director of the Institute of Industrial Information Technology (IIT), Karlsruhe Institute of Technology (KIT). His research interests include machine vision, image processing, image and information fusion, measurement technology, machine learning, artificial intelligence and their applications.